



CHORUS

This is the accepted manuscript made available via CHORUS. The article has been published as:

Imaging the Breakdown of Ohmic Transport in Graphene

Alec Jenkins, Susanne Baumann, Haoxin Zhou, Simon A. Meynell, Yang Daipeng, Kenji Watanabe, Takashi Taniguchi, Andrew Lucas, Andrea F. Young, and Ania C. Bleszynski

Jayich

Phys. Rev. Lett. **129**, 087701 — Published 17 August 2022

DOI: [10.1103/PhysRevLett.129.087701](https://doi.org/10.1103/PhysRevLett.129.087701)

Imaging the breakdown of ohmic transport in graphene

Alec Jenkins,¹ Susanne Baumann,¹ Haoxin Zhou,¹ Simon A. Meynell,¹ Daipeng Yang,¹ Kenji Watanabe,² Takashi Taniguchi,³ Andrew Lucas,⁴ Andrea F. Young,¹ and Ania C. Bleszynski Jayich^{1,*}

¹*Department of Physics, University of California, Santa Barbara CA 93106, USA*

²*Research Center for Functional Materials, National Institute for Materials Science, 1-1 Namiki, Tsukuba 305-0044, Japan*

³*International Center for Materials Nanoarchitectonics,*

National Institute for Materials Science, 1-1 Namiki, Tsukuba 305-0044, Japan

⁴*Department of Physics and Center for Theory of Quantum Matter,*

University of Colorado, Boulder CO 80309 USA

(Dated: May 13, 2022)

Ohm's law describes the proportionality of current density and electric field. In solid-state conductors, Ohm's law emerges due to electron scattering processes that relax the electrical current. Here, we use nitrogen-vacancy center magnetometry to directly image the local breakdown of Ohm's law in a narrow constriction fabricated in a high mobility graphene monolayer. Ohmic flow is visible at room temperature as current concentration on the constriction edges, with flow profiles entirely determined by sample geometry. However, as the temperature is lowered below 200 K, the current concentrates near the constriction center. The change in the flow pattern is consistent with a crossover from diffusive to viscous electron transport dominated by electron-electron scattering processes that do not relax current.

Ohm's law states that the current flow through an electrical conductor is proportional to a voltage difference across it. While this introductory textbook physics is ubiquitous in macroscopic electrical devices, Ohm's law need not hold locally at every point inside of a conductor. Specifically, Ohm's law arises only on length scales sufficiently long that microscopic scattering processes completely relax the electrical current. In an ordinary metal, impurity scattering and umklapp processes, each of which relax current, dominate the electronic dynamics; hence Ohm's law arises on scales larger than the electronic mean free path, ℓ_{mr} . In this regime, electrical transport is diffusive.

However, in low-density, low-disorder Fermi liquids, it was predicted decades ago that dynamics could be dominated by electron-electron collisions, which conserve momentum. In the regime where the electron-electron scattering length $\ell_{\text{ee}} \ll \ell_{\text{mr}}$, the momentum-conserving collisions do not completely relax the electrical current, resulting in viscous rather than diffusive transport, with current flow resembling that of a fluid [1]. Following preliminary work in the 1990s on III-V semiconductor heterostructures [2], a slew of electrical and thermal transport anomalies observed in clean graphene heterostructures have been linked to the onset of electron hydrodynamics [3–8]. Most recently, imaging studies of the Hall voltage in a small magnetic field have revealed a crossover with rising temperature from a ballistic regime, where voltage is out of equilibrium, to a regime of strong voltage equilibration [9], interpreted as evidence for a viscous regime. NV imaging of narrow graphene channels at room temperature has shown parabolic current profiles at the charge neutrality point (CNP) [10]. However, the breakdown of ohmic transport due to the onset of electron-electron dominated scattering has only been

observed indirectly in its effect on transport coefficients.

Here we use direct imaging of the current flow profile to observe the local breakdown of Ohm's law in a monolayer graphene device in which a narrow constriction has been etched. Using a scanning nitrogen vacancy (NV) center magnetometer, we image the local magnetic field above the device, related by the Biot-Savart law to the current flow profile through the constriction. These current profiles are expected to be different if the flow is limited by impurities (ohmic), electron-electron collisions (hydrodynamic), or boundary scattering (ballistic) [4, 11–14]. In the ohmic regime, current concentrates near the constriction boundaries, mathematically equivalent to the bunching of the electric field lines near the corners of a lightning rod. Hence, the presence or absence of the current bunching provides a clear means of distinguishing the transition. This clear ohmic signature in a narrow constriction contrasts with the subtle differences between ohmic and hydrodynamic or ballistic current density signatures in a long narrow channel. By directly comparing our images of current through a narrow slit and a long channel, we find that at room temperature and CNP, a viscous hydrodynamic fit to the current density in a long channel is inconsistent with the current densities measured in a narrow constriction, thus ruling out hydrodynamics at CNP in our samples, in contrast to recently published results in reference [10]. In our experiment, the relevant ratios between ℓ_{ee} , ℓ_{mr} , and the constriction width w can be tuned *in situ* via control of the carrier density and temperature. Our measurements definitively resolve the dramatic transition from ohmic to non-ohmic flow and provide evidence of a robust collision-dominated regime in which $\ell_{\text{ee}} < \ell_{\text{mr}}$.

Figure 1a-b show a schematic diagram of our experimental setup [15] and optical image of the graphene de-

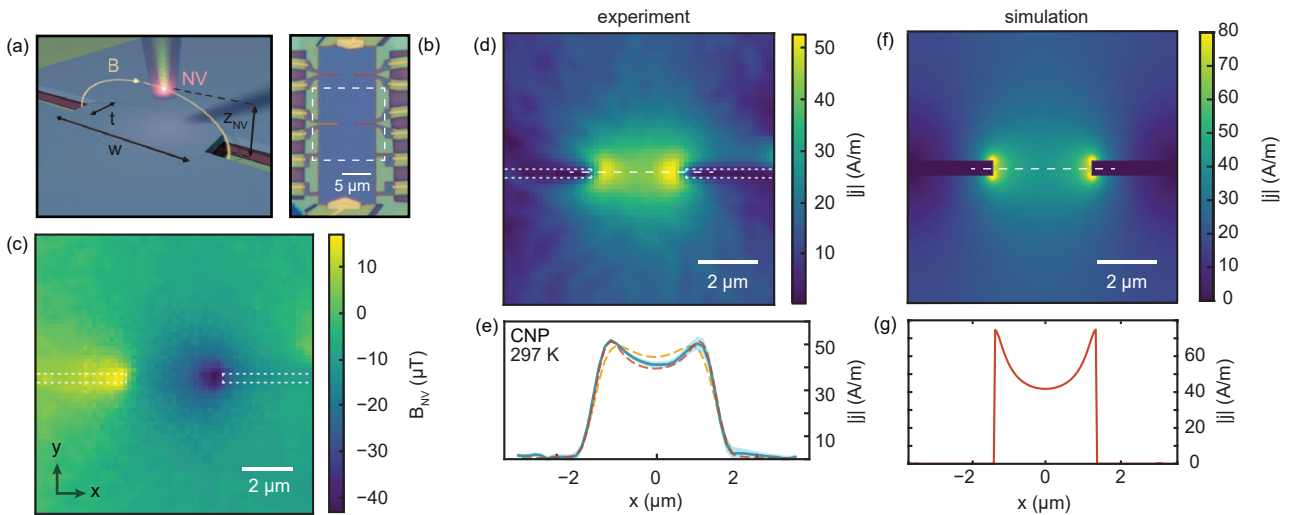


FIG. 1. **Room temperature current imaging at the charge neutrality point.** (a) Experimental setup. A diamond probe containing a 30 nm-deep, single NV center is scanned over hBN-encapsulated monolayer graphene device while current flows through an etched constriction. The stray magnetic field produced by the flowing current is measured via shifts in the NV magnetic resonance spectrum and the measured field is used to reconstruct the underlying current distribution. (b) Optical image of the graphene device. (c) Scanning NV magnetometry signal inside the area indicated by the white dashed line in (b) at room-temperature and at the charge neutrality point. The image boundaries, where the field varies slowly, are measured with sparser sampling and linear interpolation is used to fill in these regions (see supplementary information). The dotted white line shows the edges of the device as indicated by the NV fluorescence rate. (d) Reconstructed current density magnitude $|j|$ at 298 K and carrier density near the CNP ($n < 0.06 \times 10^{12} \text{ cm}^{-2}$). **The current reconstruction is performed over the entire area enclosed by the white dashed box in (b), and the image areas in (c) and (d) are cropped relative to the full image by $1.8 \mu\text{m}$ in each direction.** (e) A linecut of $|j|$ taken along the dashed white line in (d). The light blue band corresponds to the uncertainty in the reconstructed current density. The dashed red line plots the expected current profile, obtained using a parameter-free, purely ohmic model and shows good agreement with the data. The dashed orange line plots the expected constriction current profile in the small ℓ_{ee} -limit with a Gurzhi length $\ell_g = 208 \text{ nm}$ given by the fit to the measured current density profile in a long, $2.7 \mu\text{m}$ wide channel (see supplementary information). This model takes into account broadening of the features in $|j|$ due to the finite distance between the NV and the graphene. (f) The simulated ohmic current in the device without the NV filter function applied. (g) A linecut taken along the the dashed white line in (f) displays a pronounced double-peak feature indicative of ohmic transport.

vice. Current ($I = 150 \mu\text{A}$) is passed through a graphene constriction of nominal width $w = 3 \mu\text{m}$ and thickness $t = 0.4 \mu\text{m}$ etched in a monolayer of high-quality graphene encapsulated by hexagonal boron nitride. The flowing current produces a magnetic field that is sensed by the NV center. The magnetic resonance signal of the NV center is detected optically as the sample is scanned with respect to the NV at a constant height, with NV-graphene separations ranging from $z_{\text{NV}} = 140\text{--}170 \text{ nm}$ between different scans. The NV axis is oriented with a polar angle of $\theta = 50^\circ$ relative to the device normal and an azimuthal angle of $\phi = 173^\circ$ relative to the image x -axis. The resulting spatial map of the stray magnetic field (Figure 1c) is then converted using standard Fourier domain techniques [16, 17] into the total current density ($|j|$) in the vicinity of the constriction (see Figure 1d-e and Ref. [?]). The uncertainty in the reconstructed current density is dominated by two main systematic sources: the uncertainty in the NV orientation relative to the sample normal, estimated to be $\pm 4^\circ$, and the uncertainty in the NV-graphene separation, estimated to be $\pm 15 \text{ nm}$ (see

supplementary information).

We first image room temperature current flow at the charge neutrality point, shown in Figs. 1d-e. Here graphene behaves as a non-Fermi liquid, with electrical transport dominated by current-relaxing recombination of thermally excited electrons and holes. The current profile is thus expected to be ohmic [18]. Fig. 1e shows the total reconstructed current density $|j|$ across the graphene constriction. The current profile shows distinctive peaks near the constriction boundaries, consistent with expectations for ohmic transport. Indeed, the data are quantitatively well matched by a parameter-free fit to an ohmic model (dashed red line) that assumes a spatially uniform local conductivity, whose value is independently measured with transport. We compare this to the small- ℓ_{ee} , hydrodynamic limit (dashed orange line), with the Gurzhi length taken from a fit to the current density in a $2.7 \mu\text{m}$ channel geometry (see supplementary information).

The excellent agreement to the ohmic model provides strong evidence that conductivity is uniform across the

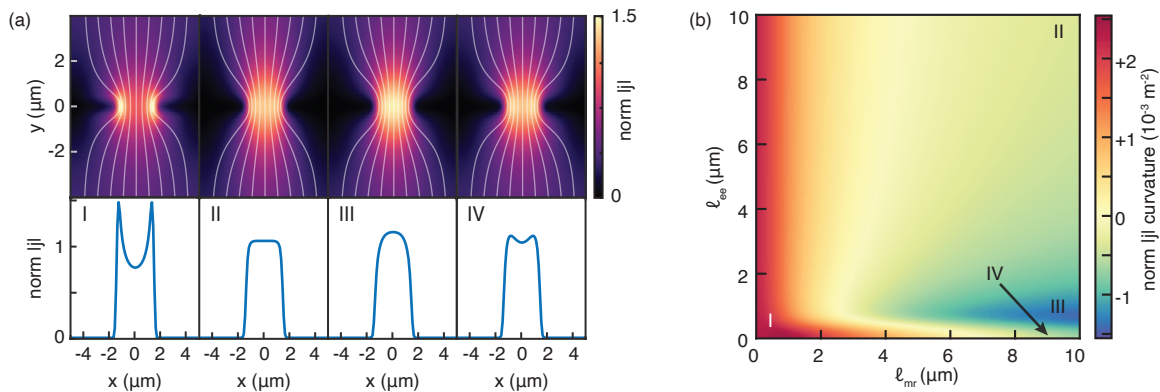


FIG. 2. **Boltzmann transport model.** (a) Four examples of current flow profiles for a slit of finite thickness and a width, $w = 3 \mu\text{m}$ and thickness $t = 0.4 \mu\text{m}$. The free parameters in the model are ℓ_{ee} and ℓ_{mr} . The current density is normalized by the average current density through the slit. Line profiles of the current across the center of the slits are shown underneath. Region I corresponds to the ohmic regime where $\ell_{mr} = \ell_{ee} \approx 0$. Region II is in the deep ballistic regime with $\ell_{mr} = \ell_{ee} = 10 \mu\text{m}$. The hydrodynamic regime is represented by III ($\ell_{ee} = 1 \mu\text{m}$, $\ell_{mr} = 10 \mu\text{m}$) where the current shape assumes a more elliptical profile. A final region, IV ($\ell_{ee} \approx 0$, $\ell_{mr} = 10 \mu\text{m}$), corresponds to when electron-electron scattering becomes so dominant that it begins to reduce the effective current relaxation length and results in viscous bunching near the slit edges. (b) The curvature of the current, $d^2|j|/dx^2$, at the center of the slit, normalized by the average current density through the slit. The changes in profiles in the regimes of II and III are subtle to resolve when uncertainty in the slit width is taken into account.

constriction at room temperature and charge neutrality, implying that other possible explanations for a nonuniform flow play a minor role [19]. It bears noting that the finite distance between NV center puts a fundamental limit on spatial resolution. The reconstructed $|j|$ in Fig. 1d-e is thus related to the physical current density via a spatial low pass filter. Figure 1f-g show the expected current distribution used to generate the fit in Fig. 1e. We conclude that at room temperature and at the CNP, transport through our device is diffusive, and momentum conserving electron-electron scattering is unimportant. This result stands in contrast to recently published results that attributed a parabolic current profile in a long channel to viscous flow at room temperature and CNP [10].

In order to understand the qualitative behavior of current flow away from the ohmic regime, we perform simulations of the quantum Boltzmann equation (QBE)[?] in our constriction geometry, which allow us to capture the effects of finite ℓ_{mr} and ℓ_{ee} . Figure 2a shows simulation results assuming $w = 3 \mu\text{m}$ for varying ℓ_{ee} and ℓ_{mr} . Evidently, current flow profiles can vary dramatically between transport regimes; in particular, the strong current concentration on the slit boundary is specific to the ohmic regime. To capture these qualitative differences in a single quantitative figure of merit, Fig. 2b shows the curvature of $|j|$ at the center of the slit plotted as a function of ℓ_{ee} and ℓ_{mr} . Deep in the ohmic regime (I) where $\ell_{mr} \ll w, \ell_{ee}$, the expected flow profile shows good agreement with the data and ohmic model fit of Fig. 1g. The ballistic regime (II) is the limit of $w \ll \ell_{mr}, \ell_{ee}$, and results in a flat current profile. Hydrodynamic effects become visible when momentum conserving colli-

sions are dominant and the momentum relaxing length scale is large compared to the device size, $\ell_{ee} \ll w < \ell_{mr}$ (III). At extremely small $\ell_{ee} \ll w^2/\ell_{mr}$ there exists a final regime (IV), deep within the hydrodynamic limit, where viscous effects are so strong that a weakly double-peaked current profile again arises, as interactions reduce the effective momentum relaxation length to $\sqrt{\ell_{ee}\ell_{mr}}$ [11, 18]. In a realistic device and measurement geometry, the ballistic and weakly hydrodynamic regions (II and III) exhibit current maxima near the constriction center and can be difficult to distinguish: the subtle quantitative differences in boundary profiles are easily obscured by the finite spatial resolution arising from the finite distance between current and magnetic field sensor.

Presented in Fig. 3a are the experimentally measured current flow profiles at several carrier densities, including charge neutrality, at both $T = 298 \text{ K}$ and $T = 128 \text{ K}$. At room temperature, the double-peaked current profile persists as the density is tuned away from charge neutrality. However, the size of the peaks is reduced with density, consistent with ℓ_{mr} increasing with density as expected from transport theories of monolayer graphene [20]. At $T = 128 \text{ K}$ and at the CNP, we again observe the double-peaked profile, indicating that charge recombination dominates scattering near the CNP even at low temperatures. However, at finite densities and $T = 128 \text{ K}$, we observe the emergence of a single-peaked current profile, an unambiguous demonstration of locally non-ohmic transport.

Because both ballistic and hydrodynamic transport are expected to be peaked in the center of the constriction, we turn to a quantitative comparison of our experimental data to the QBE simulations described above to place

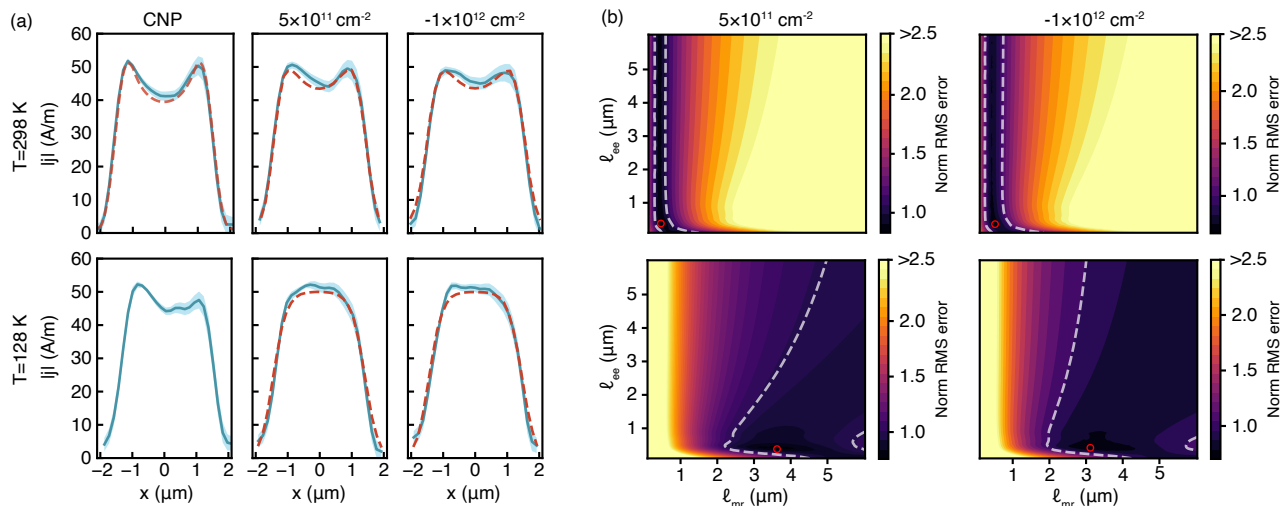


FIG. 3. Local breakdown of ohmic transport. (a) Flow profiles across the center of the slit at room temperature (top row) and at $T = 128$ K (bottom row). The red dashed line at CNP and $T = 298$ K is the current profile expected from a purely ohmic model as in Fig. 1e. The dashed red lines in the plots at $5 \times 10^{11} \text{ cm}^{-2}$ and $-1 \times 10^{12} \text{ cm}^{-2}$ are the best-fit flow profiles, with ℓ_{mr} and ℓ_{ee} given by the corresponding red circles in (b). At room temperature, ohmic double-peaked current profiles are always visible, indicating the importance of momentum-relaxing scattering processes. ℓ_{mr} can be tightly constrained at room temperature, and the current flow is insensitive to ℓ_{ee} in the regime $\ell_{\text{ee}} > 500$ nm. For lower temperatures, at finite density we observe the breakdown of the double-peaked profile and observe a rounder, single-peaked profile – the qualitative signature of the absence of strong momentum-relaxing scattering. (b) Maps of the RMS error per pixel between QBE simulations and the reconstructed current densities, normalized by the average pixel uncertainty in the current reconstruction (see supplementary information). At room temperature, the fits are consistent with diffusive transport and inconsistent with a hydrodynamic or ballistic flow. For lower temperatures, our data is inconsistent with both the deeply hydrodynamic regime and inconsistent with the diffusive regime – an indication that the device sits near the boundary between the weakly hydrodynamic and ballistic regimes. The white dashed lines correspond to fits where the RMS error per pixel is equal to the uncertainty in the current reconstruction. We take the areas bounded from above by these contours as consistent with the experimental data. The red dot corresponds to the absolute best fit in these data.

bounds on the possible values of ℓ_{ee} and ℓ_{mr} in our device. Simulations and measurements are compared over a two dimensional area of dimensions 4.0×1.6 microns centered on the constriction (see [?]). The dashed red lines in Fig. 3a at carrier densities $n = 5 \times 10^{11} / \text{cm}^2$ and $n = -1 \times 10^{12} / \text{cm}^2$ are slices of through the best-fit current patterns of the QBE simulations. At the CNP and 298 K, we find good agreement between a purely ohmic model (red dashed line) and a slice through the reconstructed current density.

Figure 3b shows the root mean square (RMS) residual per pixel of the fit normalized by the average uncertainty in the current reconstruction, plotted as a function of the simulation input parameters ℓ_{ee} and ℓ_{mr} . The white dashed lines correspond to contours with average residuals equal to the average current reconstruction uncertainty (see supplementary information). We take areas of the parameter space bounded from above by these contours (darker shades in Fig. 3b) as consistent with experimental data.

At room temperature, magnetometry data constrain $\ell_{\text{mr}} \lesssim 1 \mu\text{m}$, while providing no constraint on the value of ℓ_{ee} . This is consistent with estimates for scattering by momentum-relaxing phonons, which dominate scat-

tering on experimentally relevant length scales resulting in ohmic flow. Best fit regions are markedly different at $T = 128$ K, and most consistent with the crossover regime intermediate between hydrodynamic and ballistic flow. At $T = 128$ K, the average RMS residual is minimal for $\ell_{\text{ee}} = 0.4 \mu\text{m}$ and $\ell_{\text{mr}} = 3.1 \mu\text{m}$ for both $n = 5 \times 10^{11} / \text{cm}^2$ and $n = -1 \times 10^{12} / \text{cm}^2$. However, larger values of ℓ_{ee} and ℓ_{mr} are only weakly constrained, primarily due to uncertainty in the precise nature of the boundary conditions, as well as uncertainty in the constriction width. An independent check on these fits can be obtained from measurements of the conductivity σ in the same device (see [?]), from which we extract the mean free path $\ell_{\text{mfp}} = h\sigma / 2k_{\text{F}}e^2$, where $k_{\text{F}} = \sqrt{\pi n}$ is the Fermi wavevector. In the Fermi liquid regime, ℓ_{mfp} approximates ℓ_{mr} . We find that at both 298 K ($\ell_{\text{mfp}} \approx 0.9 \mu\text{m}$) and 128 K ($\ell_{\text{mfp}} \approx 4.3 \mu\text{m}$) the measured mean free path agrees with the momentum relaxation length obtained from the NV magnetometry fits. Our data thus completely rule out both the strongly interacting hydrodynamic regime (IV) and the ohmic regime (I).

In order to conclusively resolve the subtle differences in flow patterns in the hydrodynamic/ballistic crossover

regime, a geometry better suited to measuring these differences or a sharper understanding of the realized boundary conditions will be required. However, our results, when taken together with those of Ref. [9], suggest that monolayer graphene hosts a weakly interacting hydrodynamic regime at intermediate temperatures, manifesting in strongly modified local current and voltage distribution patterns. Additionally, in this work we use a 2-dimensional geometry designed to minimize the importance of uncontrolled scattering at the etched walls of the device in order to rule out spurious flow patterns. Ref. [9] explores hydrodynamic effects in a 1-dimensional geometry that can be susceptible to effects from imperfect boundaries.

Looking forward, locally resolved current measurements may be useful in conclusively resolving hydrodynamic effects (or the lack thereof) in more exotic materials [21, 22]. More broadly, these techniques provide a powerful method for visualizing electronic dynamics normally invisible in bulk resistivity measurements.

ACKNOWLEDGMENTS

The authors acknowledge discussions with L. Levitov, and thank J. Sanchez-Yamagishi for comments on the manuscript. This work was primarily supported by the National Science Foundation under award DMR-1810544. KW and TT acknowledge support from the Elemental Strategy Initiative conducted by the MEXT, Japan and the CREST (JPMJCR15F3), JST. AFY acknowledges the support of the David and Lucile Packard Foundation. AL acknowledges the support of the Alfred P. Sloan Foundation. SAM acknowledges the support of the Natural Sciences and Engineering Research Council of Canada (NSERC), [AID 516704-2018].

* To whom correspondence should be addressed. E-mail: ania@physics.ucsb.edu

- [1] R. N. Gurzhi, Soviet Physics Uspekhi **11**, 255 (1968).
- [2] M. J. De Jong and L. W. Molenkamp, Physical Review B **51**, 13389 (1995).
- [3] J. Crossno, J. K. Shi, K. Wang, X. Liu, A. Harzheim, A. Lucas, S. Sachdev, P. Kim, T. Taniguchi, K. Watanabe, T. A. Ohki, and K. C. Fong, Science **351**, 1058 (2016).
- [4] R. Krishna Kumar, D. A. Bandurin, F. M. Pellegrino, Y. Cao, A. Principi, H. Guo, G. H. Auton, M. Ben Shalom, L. A. Ponomarenko, G. Falkovich, K. Watanabe, T. Taniguchi, I. V. Grigorieva, L. S. Levitov, M. Polini, and A. K. Geim, Nature Physics **13**, 1182 (2017).
- [5] P. Gallagher, C.-S. Yang, T. Lyu, F. Tian, R. Kou, H. Zhang, K. Watanabe, T. Taniguchi, and F. Wang, Science, eaat8687 (2019).
- [6] A. I. Berdyugin, S. G. Xu, F. M. D. Pellegrino, R. K. Kumar, A. Principi, I. Torre, M. B. Shalom, T. Taniguchi, K. Watanabe, I. V. Grigorieva, M. Polini, A. K. Geim, and D. A. Bandurin, Science **364**, 162 (2019).
- [7] D. A. Bandurin, A. V. Shytov, L. S. Levitov, R. K. Kumar, A. I. Berdyugin, M. B. Shalom, I. V. Grigorieva, A. K. Geim, and G. Falkovich, Nature Communications **9**, 1 (2018).
- [8] D. A. Bandurin, I. Torre, R. K. Kumar, M. B. Shalom, A. Tomadin, A. Principi, G. H. Auton, E. Khestanova, K. S. Novoselov, I. V. Grigorieva, L. A. Ponomarenko, A. K. Geim, and M. Polini, Science **351**, 1055 (2016).
- [9] J. A. Sulpizio, L. Ella, A. Rozen, J. Birkbeck, D. J. Perello, D. Dutta, M. Ben-Shalom, T. Taniguchi, K. Watanabe, T. Holder, R. Queiroz, A. Principi, A. Stern, T. Scaffidi, A. K. Geim, and S. Ilani, Nature **576**, 75 (2019).
- [10] M. J. Ku, T. X. Zhou, Q. Li, Y. J. Shin, J. K. Shi, C. Burch, L. E. Anderson, A. T. Pierce, Y. Xie, A. Hamo, U. Vool, H. Zhang, F. Casola, T. Taniguchi, K. Watanabe, M. M. Fogler, P. Kim, A. Yacoby, and R. L. Walsworth, Nature **583**, 537 (2020).
- [11] L. Levitov and G. Falkovich, Nature Physics **12**, 672 (2016).
- [12] H. Guo, E. Ilseven, G. Falkovich, and L. S. Levitov, Proceedings of the National Academy of Sciences **114**, 3068 (2017).
- [13] H. Guo, Bachelor's thesis, Massachusetts Institute of Technology, Department of Physics (2018).
- [14] M. Shavit, A. Shytov, and G. Falkovich, Physical Review Letters **123**, 26801 (2019).
- [15] M. Pelliccione, A. Jenkins, P. Ovarthaiyapong, C. Reetz, E. Emmanouilidou, N. Ni, and A. C. Bleszynski Jayich, Nature Nanotechnology **11**, 700 (2016).
- [16] B. J. Roth, N. G. Sepulveda, and J. P. Wikswo, Journal of Applied Physics **65**, 361 (1989).
- [17] K. Chang, A. Eichler, J. Rhensius, L. Lorenzelli, and C. L. Degen, Nano Letters **17**, 2367 (2017).
- [18] A. Lucas and K. C. Fong, Journal of Physics: Condensed Matter **30**, 053001 (2018).
- [19] P. G. Silvestrov and K. B. Efetov, Physical Review B - Condensed Matter and Materials Physics **77**, 10.1103/PhysRevB.77.155436 (2008).
- [20] S. Das Sarma, S. Adam, E. H. Hwang, and E. Rossi, Reviews of Modern Physics **83**, 407 (2011).
- [21] P. J. Moll, P. Kushwaha, N. Nandi, B. Schmidt, and A. P. Mackenzie, Science **351**, 1061 (2016).
- [22] J. Gooth, F. Menges, N. Kumar, V. Süß, C. Shekhar, Y. Sun, U. Drechsler, R. Zierold, C. Felser, and B. Gotsmann, Nature Communications **9**, 4093 (2018).
- [23] See Supplemental Material [url] for a description of device fabrication, our magnetometry methods, details on the Boltzmann Transport theory, and a comparison between the slit and channel geometries. The supplement includes the references listed below.
- [24] L. Wang, I. Meric, P. Y. Huang, Q. Gao, Y. Gao, H. Tran, T. Taniguchi, K. Watanabe, L. M. Campos, D. A. Muller, J. Guo, P. Kim, J. Hone, K. L. Shepard, and C. R. Dean, Science **342**, 614 (2013).
- [25] A. A. Zibrov, C. Kometter, H. Zhou, E. M. Spanton, T. Taniguchi, K. Watanabe, M. P. Zaletel, and A. F. Young, Nature **549**, 360 (2017).
- [26] P. J. Zomer, M. H. D. Guimarães, J. C. Brant, N. Tombros, and B. J. Van Wees, Applied Physics Letters

- 105**, 013101 (2014).
- [27] R. S. Schoenfeld and W. Harneit, *Physical Review Letters* **106**, 10.1103/PhysRevLett.106.030802 (2011).
- [28] E. A. Lima and B. P. Weiss, *Journal of Geophysical Research: Solid Earth* **114**, 10.1029/2008JB006006 (2009).
- [29] F. Dolde, H. Fedder, M. W. Doherty, T. Nöbauer, F. Rempp, G. Balasubramanian, T. Wolf, F. Reinhard, L. C. Hollenberg, F. Jelezko, and J. Wrachtrup, *Nature Physics* **7**, 459 (2011).
- [30] P. J. Ledwith, H. Guo, and L. Levitov, *Annals of Physics* **411**, 10.1016/j.aop.2019.167913 (2019).
- [31] A. Lucas, *Physical Review B* **95**, 115425 (2017).